Check for updates

Microstructure–mechanical properties of Ag⁰/Au⁰ doped K–Mg–Al–Si–O–F glass-ceramics

Mrinmoy Garai, [ID] *[a] Arianit A. Reka, [ID] [b] Basudeb Karmakar[a] and Atiar R. Molla[a]

In understanding the catalytic efficacy of silver (Ag⁰) and gold (Au⁰) nanoparticles (NPs) on glass-ceramic (GC) crystallization, the microstructure–machinability correlation of a SiO_2–MgO–Al_2O_3–B_2O_3–K_2O–MgF_2 system is studied. The thermal parameters *viz.*, glass transition temperature (T_g) and crystallization temperature (T_c) were extensively changed by varying NPs (*in situ* or *ex situ*). Tc was found to be increased (T_c = 870–875 °C) by 90–110 °C when *ex situ* NPs were present in the glass system. Under controlled heat-treatment at 950 ± 10 °C, the glasses were converted into glass-ceramics with the predominant presence of crystalline phase (XRD) fluorophlogopite mica, [$KMg_3(AlSi_3O_{10})F_2$]. Along with the secondary phase enstatite ($MgSiO_3$), the presence of Ag and Au particles (FCC system) were identified by XRD. A microstructure containing spherical crystallite precipitates (~50–400 nm) has been observed through FESEM in *in situ* doped GCs. An *ex situ* Ag doped GC matrix composed of rock-like and plate-like crystallites mostly of size 1–3 μm ensured its superior machinability. Vicker's and Knoop microhardness of *in situ* doped GCs were estimated within the range 4.45–4.61 GPa which is reduced to 4.21–4.34 GPa in the *ex situ* Ag system. Machinability of GCs was found to be in the order, *ex situ* Ag > *ex situ* Au ~ *in situ* Ag > *in situ* Au. Thus, the *ex situ* Ag/Au doped SiO_2–MgO–Al_2O_3–B_2O_3–K_2O–MgF_2 GC has potential for use as a machinable glass-ceramic.

1. Introduction

Fluormica glass-ceramics are polycrystalline materials containing a residual silicate (Si–O–Si) glass matrix with a dispersed crystalline phase.[1–3] They are considered machinable as they can be readily milled, drilled, turned or cut without resorting to diamond tipped tools.[2–4] The superior machinability of such fluormica glass-ceramics is due to their unique microstructure consisting of plate-like fluorophlogopite [$KMg_3(AlSi_3O_{10})F_2$] crystals that impinge on one another.[4,5] This type of microstructure possesses enough capability to prevent fracture by offering preferential cleavage along the [001] crystalline plane.[5,6] Moreover, the layered structure of [$KMg_3(AlSi_3O_{10})F_2$] crystallites allows easy splitting along the planes of the flat structural network, while splitting across the flat crystal network is hard due to the possibility of bending and shifting along the splitting planes.[7,8]

There is increasing interest in [$KMg_3(AlSi_3O_{10})F_2$] based glass-ceramics for dental crowns, onlays and inlays, particularly with the widespread usage of CAD–CAM within dental surgery.[9–12] These applications using mica based glass-ceramics are directly dependent on their machinability which is strongly influenced by hardness of the GC.[13,14] The following equation[14]

indicates the relationship between Hardness (H) and machinability parameter (m):

$$m = 0.643 - 0.122H \qquad (1)$$

The mechanical properties like microhardness of mica glass-ceramics are strongly affected by crystallite particle size, amount of precipitated mica crystals, their strength and volume fraction of the crystalline matrix.[15–18] Behraznia *et al.*[14] argued that machinability of mica glass-ceramics is widely varied with effective crystallinity which is a combining parameter of aspect ratio of crystals and the volume fraction.[4] They[14] explicated that, as the mica volume fraction increases there is a reducing need to have a high aspect ratio in order to achieve a high effective crystallinity. In case of lower volume fraction mica glass-ceramics, a high aspect ratio (>10) is required in order to achieve better machinability.[4,5,14] The commercial glass-ceramic Macor® possess the aspect ratio >20 and a relatively low crystal volume fraction.[5,14]

Thus, the microstructural parameters *i.e.* crystallinity, aspect ratio and volume fraction altogether control machinable properties of [$KMg_3(AlSi_3O_{10})F_2$] glass-ceramics. Crystallization (or devitrification) in vitreous systems like SiO_2–MgO–Al_2O_3–K_2O–B_2O_3–F (with highly viscous nature) process is generally leaded by two kinetic processes: (i) phase separation by nucleation and growth and (ii) spinodal decomposition.[1,7] To obtain the fine-grained microstructures, it is essential to ensure that

[a]*Specialty Glass Division, CSIR-Central Glass & Ceramic Research Institute (CGCRI), Kolkata, India. E-mail: mrinmoygarai@yahoo.in*

[b]*Department of Chemistry, Faculty of Natural Sciences and Mathematics, University of Tetova, Blvd Ilinden n. n., 1200 Tetovo, Republic of North Macedonia*
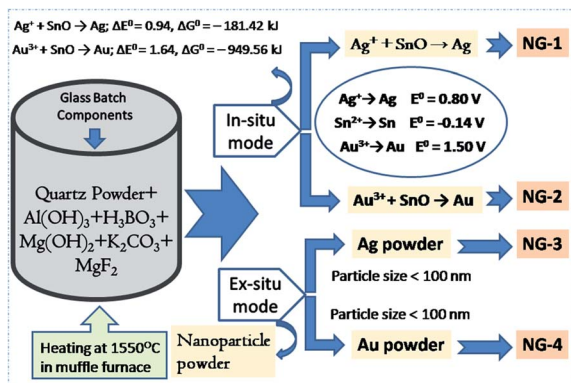
Reduction of Ag^+ into Ag and Au^{3+} into Au were then happened during final heating to cooling time through the following mechanism:

$$Sn^{2+}/Sn + Ag^+ \rightarrow Sn^{4+}/Sn^{2+} + Ag^0 \qquad (2)$$

$$Sn^{2+}/Sn + Au^{3+} \rightarrow Sn^{4+}/Sn^{2+} + Au^0 \qquad (3)$$
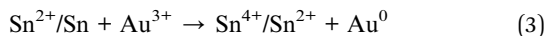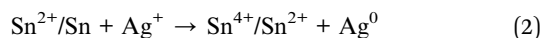
The free energy change $(\Delta G°)$ for those reductions is calculated from respective cell potential $(\Delta E°)$.[22]

$$Ag^+ + SnO \rightarrow Ag; \Delta E° = 0.94, \Delta G° = -181.42 \text{ kJ} \qquad (4)$$

$$Au^{3+} + SnO \rightarrow Au; \Delta E° = 1.64, \Delta G° = -949.56 \text{ kJ} \qquad (5)$$
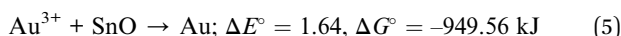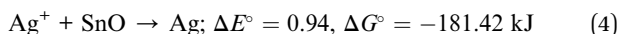
For a reaction to occur spontaneously, the free energy change $(\Delta G°)$ should be negative. From the above two eqn (4) and (5), it is seen that $\Delta G°$ value for reduction of silver $(Ag^+ \rightarrow Ag)$ and gold $(Au^{3+} \rightarrow Au)$ is strongly negative. In this way the *in situ* NPs were doped in SiO_2–Al_2O_3–MgO–K_2O–B_2O_3–MgF_2 glass.

For *ex situ* nanoparticle doping (NG-3 & NG-4), the Ag- and Au-nanometal powder (particle size <100 nm) were directly mixed (Fig. 1) into SiO_2–Al_2O_3–MgO–K_2O–B_2O_3–MgF_2 glass batch mixture (Table 1).

2.2 Melt-quenching of glasses

About 100 g raw materials were used (details about raw materials presented in Table 1), for synthesis of various nanoparticle doped precursor glasses (*i.e.* NG-1 to NG-4) based on the component system SiO_2–Al_2O_3–MgO–K_2O–B_2O_3–MgF_2 (composition shown in Table 2), were weighed, thoroughly mixed and melted in a platinum (Pt) crucible at 1550 ($\pm$10) °C for 2 h with intermittent stirring for 15 s using a silica glass rod. Finally, each glass melt was poured onto a pre-heated steel mold to obtain the quenched glass block. Fig. 1 depicts the schematic diagram for synthesis of nanoparticle doped glasses. The quenched NG glass blocks were annealed in a muffle furnace at 620 ($\pm$10) °C for 2 h to remove the internal thermal stresses developed in the glass followed by natural cooling to room temperature.

2.3 Controlled crystallization

The as-annealed SiO_2–Al_2O_3–MgO–K_2O–B_2O_3–MgF_2 glasses were cut into pieces for necessary characterizations as well as heat-treatment for crystallization. The glass pieces were allowed to heat-treatment at temperature 950 ($\pm$10) °C for ~4 h duration so that sufficient time is attained for crystallization. The as-annealed and heat-treated glass blocks were cut, grinded on

silicon carbide and polished with cerium oxide powders into required dimensions to carry out the necessary characterizations.

2.4 Characterization of glasses and glass-ceramics

In order to estimate the glass transition temperature (T_g) and crystallization temperature (T_c), differential scanning calorimetry (DSC) experiment using precursor SiO_2–Al_2O_3–MgO–K_2O–B_2O_3–MgF_2 glass powders (particle size < 60 μm) was carried out in the temperature range 30–1200 °C in nitrogen atmosphere at heating rate 20 °C min^{-1} with a NETZSCH instrument (Model STA 449 Jupiter F3, NETZSCH-Gerätebau GmbH, Selb, Germany).

The densities (ρ) of the glass samples were determined by the standard Archimedes principle. The measurements were done using single pan balance and distilled water (H_2O) as an immersion liquid. The density (ρ) was obtained from the relation:

$$\rho = \frac{ad}{(a-b)} \qquad (6)$$

where '*a*' is the weight of the glass sample in air, '*b*' is the weight of the glass sample when suspended in distilled water (considering density of water, $d = 0.997604$ g cm^{-3} at 25 °C).

The X-ray diffraction (XRD) of the glasses and heat-treated glass-ceramics were investigated using an XPERTPRO MPD diffractometer (PANalytical, Almelo, Netherlands) operating with Ni-filtered CuKα ($\lambda = 1.5406$ Å) radiation as the X-ray source irradiated at 40 kV and 40 mA. The scan range was 5°–90° with a step size of 0.05° at room temperature (~25 °C).

The crystallization characteristics and microstructural morphology of SiO_2–Al_2O_3–MgO–K_2O–B_2O_3–MgF_2 glass-ceramics was examined with a field-emission scanning electron microscope (FESEM model S430i, LEO, CEA, USA). Prior to the FESEM investigations, the glass-ceramic samples were polished and chemically etched by immersion into 2 vol% aqueous HF solution for 7 min. To dictate the existing elements (K, Mg, Al, Si, O and F) in the glass-ceramic matrix, qualitative elemental composition analysis was performed using energy dispersive X-ray (EDX) analysis using the EDX detector attached with FESEM microscope.

The micro hardness of all the polished SiO_2–Al_2O_3–MgO–K_2O–B_2O_3–MgF_2 glass-ceramics were determined using micro indentation hardness testing systems (Clemex CMT, Longueli, Canada) equipped with a conical Vickers indenter. Average of ten indentations was taken for each sample applying 200 gf load for dwell time = 5 s. The diagonals of the different indents were measured using the optical microscope attached with the instrument and consequently the hardness values were calculated using the standard eqn (7) and (8) for the Vickers and Knoop geometries respectively.

$$H_V = \frac{1.854P}{d^2} \qquad (7)$$

$$H_K = \frac{1.854P}{C_p L^2} \qquad (8)$$

Table 2 Composition (wt%) of different precursor nanoparticle doped SiO_2–Al_2O_3–MgO–K_2O–B_2O_3–MgF_2 glasses

Glass	SiO_2	Al_2O_3	MgO	K_2O	B_2O_3	MgF_2	SnO	Excess
NG-1	39	16	12	10	11	12	0.3	Ag = 0.2 (*in situ*)
NG-2	39	16	12	10	11	12	0.3	Au = 0.2 (*in situ*)
NG-3	39	16	12	10	11	12	—	Ag = 0.2 (*ex situ*)
NG-4	39	16	12	10	11	12	—	Au = 0.2 (*ex situ*)
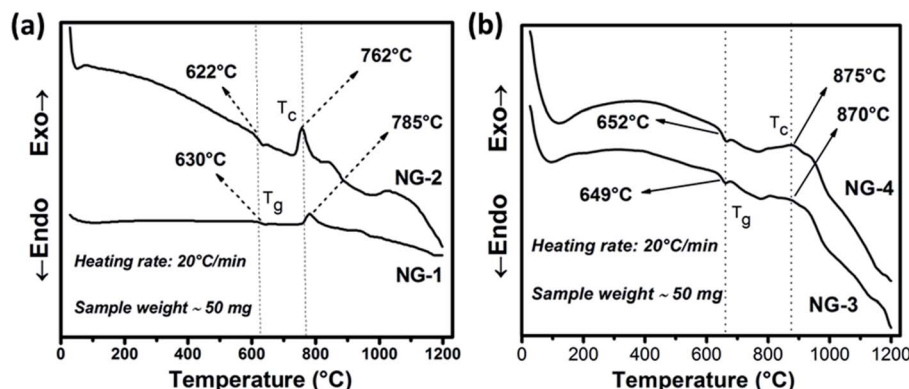
Fig. 2 DSC curves of *in situ* (a) and *ex situ* (b) Ag/Au nanoparticle doped SiO_2–Al_2O_3–MgO–K_2O–B_2O_3–MgF_2 glasses.

Table 3 DSC thermal properties (°C) of different precursor nanoparticle doped SiO_2–Al_2O_3–MgO–K_2O–B_2O_3–MgF_2 glasses[a]

Glass	T_g	T_x	T_c
NG-1	630 ± 2	748 ± 2	785 ± 2
NG-2	622 ± 2	732 ± 2	762 ± 2
NG-3	649 ± 2	780 ± 2	870 ± 2
NG-4	652 ± 2	763 ± 2	875 ± 2

[a] T_g = glass transition temperature; T_g = crystallization onset temperature; T_c = crystallization temperature.

where, H_V and H_K are the Vickers and Knoop hardness numbers in kg mm^{-2}. P is the normal load in kg, d is the average diagonal length of the indentation in mm, L is length of indentation along its long axis and C_p is the correction factor related to the shape of the indentor (=0.070279). Here, the hardness value obtained/100.1 = hardness (H) in GPa. The machinability parameter (m) was determined using the eqn (1) *i.e.* $m = 0.643 - 0.122H$.[14] The machinability parameter 'm' is important to characterize the machinable mica glass-ceramics.

3. Results and discussion

3.1. DSC thermal properties of SiO_2–Al_2O_3–MgO–K_2O–B_2O_3–MgF_2 glasses

Controlled heat-treatment facilitated the glass to glass-ceramic phase transformation with containing the desired crystalline phase. From differential scanning calorimetry (DSC) experiment the optimum heat-treatment temperature was selected. The DSC thermograms of the investigated nanoparticle doped SiO_2–Al_2O_3–MgO–K_2O–B_2O_3–MgF_2 glasses are shown in Fig. 2. Glass transition (T_g) temperature is the characteristic feature of the first endothermic minima in DSC thermogram whereas the exothermic peaks correspond to the crystallization temperatures (T_c). As is evident from Fig. 2a, in the DSC thermogram of NG-1 glass, a slight endothermic peak is started to at ~617 °C and ends at ~645 °C. For the other glasses containing *in situ* generated Au (NG-2 in Fig. 2a), *ex situ* doped Ag (NG-3 in Fig. 2b) and *ex situ* doped Au (NG-4 in Fig. 2b); the first endothermic peak starts to appear at about ~628, ~644 and ~642 °C and reached the bottom at approximately ~638, ~668 and ~665 °C, respectively. From the onset of endothermic hump T_g value was estimated 630 ± 2 and 622 ± 2 °C for NG-1 and NG-2 glasses, respectively. As is seen from Table 3, T_g value increased in NG-3

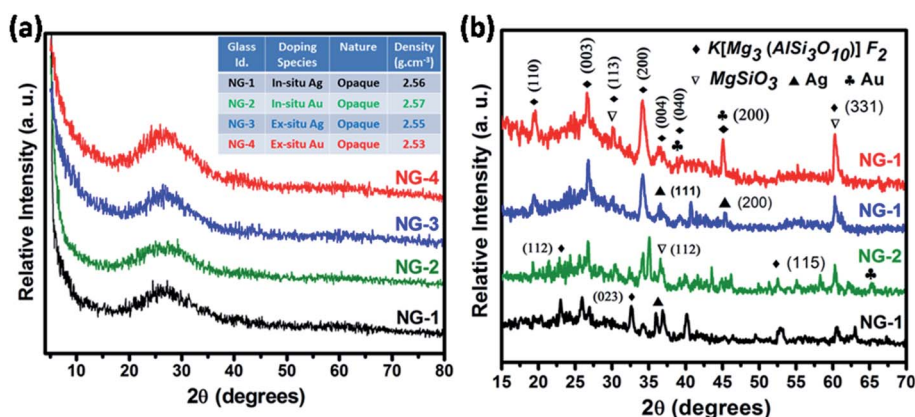**Fig. 3** X-ray diffraction (XRD) pattern of (a) SiO_2–Al_2O_3–MgO–K_2O–B_2O_3–MgF_2 glasses and (b) corresponding glass-ceramics heat-treated at 950 °C.

and NG-4 glasses because of more stable glass network in presence of *ex situ* doped Ag and Au nanoparticles.

The exothermic peak starts to appear in the DSC thermogram (Fig. 1a), at ~748 and ~732 °C (T_x) for NG-1 and NG-2 glasses, respectively, indicating onset of crystallization. For *ex situ* coinage nanometal doped glasses *i.e.*, NG-3 and NG-4, this exotherm is started at ~780 and ~763 °C (T_x), respectively. Difference between the T_x and T_g describe thermal stability (TS) of glass phase.[20–23]

$$TS = T_x - T_g \tag{9}$$

For NG-1, NG-2, NG-3 and NG-4 glasses, TS is calculated as 111, 110, 131 and 114 °C, respectively. Such TS value is rather low for a glass to be thermally stable, also it indicates that the nucleation and growth process may be initiated well before the crystallization peaks obtained in DSC studies. Ag-Being the 4d transition metal has lower atomic size than Au-(5d) and hence it can accommodate itself in the glass matrix more comfortably. So, the glass stability of NG-1 and NG-3 glasses (*in situ* and *ex situ* silver) is more than that of NG-2 and NG-4 glasses (*in situ* and *ex situ* gold). For NG-1, NG-2, NG-3 and NG-4 glasses, the

first exothermic peak *i.e.* T_C (Fig. 2) is observed at 785, 762, 870 and 875 °C, respectively. So, the primary crystallization temperature increased ~80–110 °C on doping of *ex situ* silver and gold nanoparticle instead of *in situ* generated silver and gold (Table 2). Moreover, the first exothermic peak obtained NG-1 and NG-2 glasses is sharper than that of NG-2/NG-3 glasses that signifies that *in situ* nanoparticles doped glass-ceramics are formed because of either single-phase crystallization or an almost simultaneous precipitation of different crystalline phases after heat treatment.

3.2 Crystalline phases in SiO_2–Al_2O_3–MgO–K_2O–B_2O_3–MgF_2 glass-ceramics

The glassy nature of precursor glasses and crystalline nature of corresponding glass-ceramics after heat-treatment at 950 °C was identified by XRD study depicted in Fig. 3. No crystalline phase developed in melt-quenched (1550 °C) SiO_2–Al_2O_3–MgO–K_2O–B_2O_3–MgF_2 glass was confirmed from Fig. 3a. As provided in the inset of Fig. 3a, the density of nanoparticle doped glasses have been found 2.53–2.57 g cm^{-3}. The XRD pattern of GCs heat-treated at 950 °C is presented in Fig. 3b. Three major

Table 4 XRD peaks and corresponding planes of different crystalline phases developed in studied machineable glass-ceramic

Peak position (2θ) (degree)	Corresponding planes	Crystalline phase (chemical formula)	JCPDS file no.
19.4, 23.3, 26.6, 30.3, 32.7, 34.3, 36.6, 39.3, 45.1, 52.5, 60.5, 62.9	(110), (112), (003), (113), (023), (200), (004), (040), (111), (115), (331), (261)	Fluorophlogopite ($KMg_3AlSi_3O_{10}F_2$)	71-1542
30.1, 36.7, 60.4	(321), (112), (650)	Enstatite ($MgSiO_3$)	83-2057
36.5, 44.8, 64.7	(111), (200), (220)	Silver particle (Ag)	01-1164
38.8, 45.1, 65.2	(111), (200), (220)	Gold particle (Au)	02-1095

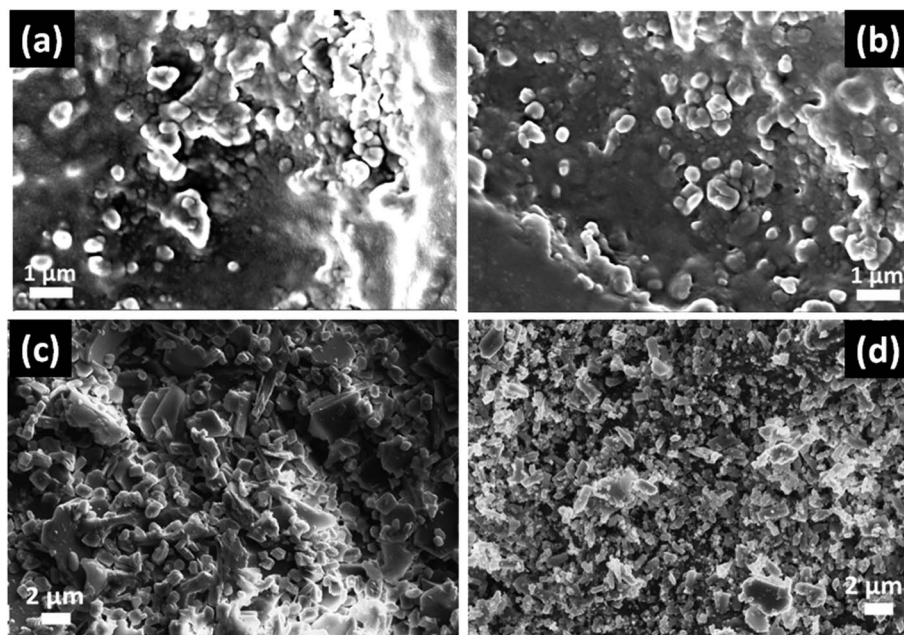**Fig. 4** FESEM photomicrograph of (a) NG-1, (b) NG-2, (c) NG-3 and (d) NG-4 glass-ceramics heat-treated at 950 °C (SiO_2–Al_2O_3–MgO–K_2O–B_2O_3–MgF_2 samples polished and chemically etched by 2 vol% aqueous HF solution for 7 min).

crystalline peaks appeared at (2θ) ~26.6°, 32.7° and 60.5° is almost similar for NG-1 to NG-4 glass-ceramics. As summarized in Table 4, that three major peaks correspond to the crystalline planes (003), (023) and (331) of fluorophlogopite mica $[KMg_3(AlSi_3O_{10})F_2]$, JCPDS file number 71-1542 (molecular weight = 421.24, monoclinic system (end-centered) with lattice parameter: $a = 5.299$, $b = 9.188$ and $c = 10.13$. Other crystalline planes *i.e.* (110), (112), (113), (200), (004), (040), (111), (115) and (261) indexed at (2θ) 19.4°, 23.3°, 30.3°, 34.3°, 36.6°, 39.3°, 45.1°, 52.5° and 62.9° are also observed due to the formation of fluorophlogopite phase where large 12-coordinated K^+ ions are electrovalent bonded with strongly bound alumino-silicate sheets $[Mg_3(AlSi_3O_{10})F_2]^-$. From Fig. 3b it is clearly observed that more intense crystalline planes for fluorophlogopite are obtained in NG-3 and NG-4 glass-ceramics, and that is attributed to the presence of *ex situ* doped nanoparticles. Efficient nucleation by heterogeneous phase

separation with the aid of such metallic nuclei was first achieved by Stookey[21] in precipitating the metallic nuclei throughout the glass. Since those metals are relatively insoluble in silicate (Si–O–Si) glass, heterogeneous nucleating sites are contentedly initiated by addition of a small amount of the metal.[21,26,27] In the studied SiO_2–Al_2O_3–MgO–K_2O–B_2O_3–MgF_2 glass the Ag- and Au-nanoparticles catalyzed the formation of $[KMg_3(AlSi_3O_{10})F_2]$ during the heat-treatment. However, a secondary crystalline phase was identified by the XRD peaks positioned at (2θ) 30.1°, 36.7° and 60.4° corresponding to (321), (112) and (650), respectively for the development of enstatite ($MgSiO_3$), JCPDS file no. 83-2057 (orthorhombic, primitive).

In the XRD pattern of mica based glass-ceramics, the presence of several overlapping peaks becomes difficult to determine because of their low intensity.[23,24] In the glass-ceramics heat-treated at 950 °C, the presence of Ag- and Au-
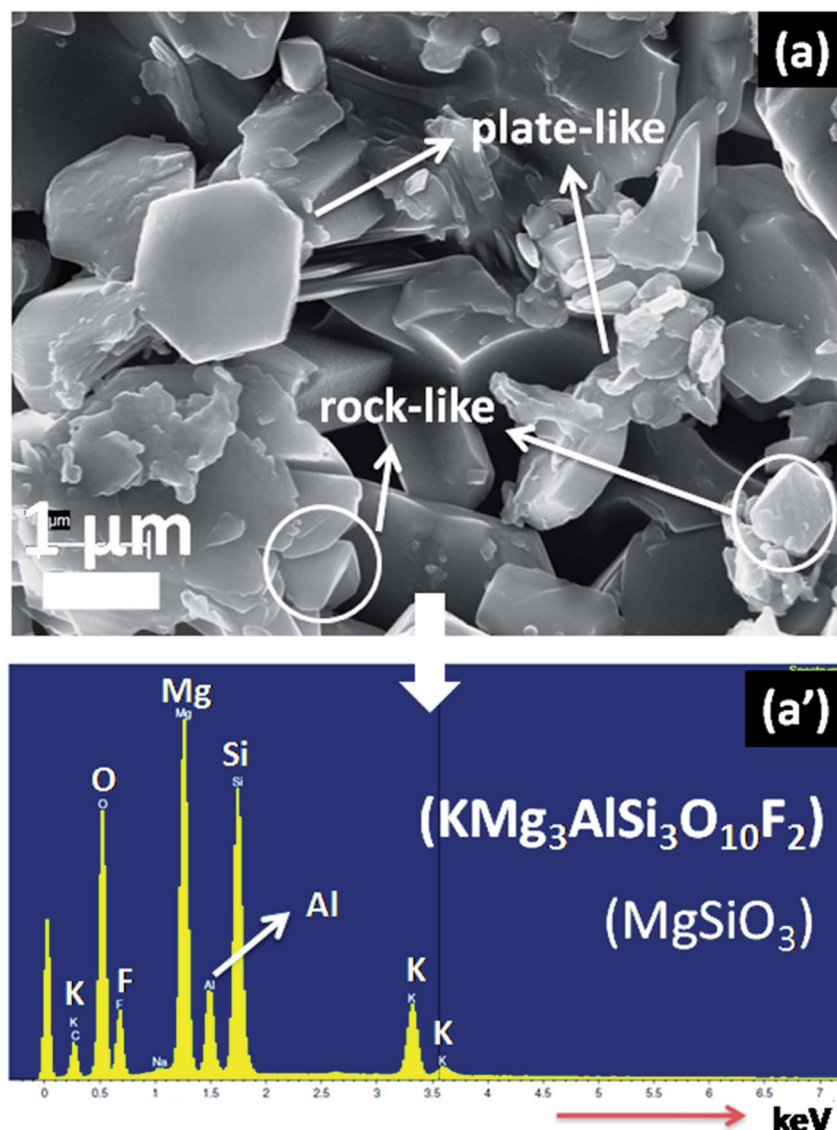

Fig. 5 Representative FESEM photomicrograph (a) and EDX pattern (a') of *ex situ* Ag-doped SiO_2–Al_2O_3–MgO–K_2O–B_2O_3–MgF_2 glass-ceramic (NG-3) heat-treated at 950 °C (sample is polished and chemically etched by 2 vol% aqueous HF solution for 7 min).

nanoparticles were also identified by XRD study. As seen from Fig. 3b, the Ag-nanoparticle has been identified at the characteristic peaks (2θ) of 36.5° and 44.8° corresponding to (111) and (200) and (220) planes (JCPDS file no. 01-1164, face centered cubic, lattice parameter a = 4.079). The presence of Au-nanoparticle was identified at the peak positions (2θ) of 38.8°, 45.1° and 65.2° corresponding to (111), (200) and (220) crystalline planes; JCPDS file number 02-1095, face centered cubic lattice, lattice parameter a = 4.068. Fig. 3b clearly shows the crystalline peaks corresponding to fluorophlogopite formation in NG-3 & NG-4 is more intensified compare to NG-1 & NG-2. This is due to the catalytic activity of Ag- and Au-particles as their lattice parameter is closely matched (within ±15%) with that of fluorophlogopite phase.

3.3 Morphology in SiO_2–Al_2O_3–MgO–K_2O–B_2O_3–MgF_2 glass-ceramics

In Fig. 4, the FESEM morphology of HF-etched surface of the SiO_2–Al_2O_3–MgO–K_2O–B_2O_3–MgF_2 glass-ceramics heat-treated at 950 °C are shown. Fig. 4a and b represents the microstructure of NG-1 and NG-2 glass-ceramics which contains *in situ* generated nanoparticles whereas Fig. 4c and d depicts the microstructure of *ex situ* nanoparticle doped glass-ceramics. The crystallite particles randomly dispersed in all these microstructures are identified as fluoro-phlogopite mica [$KMg_3(AlSi_3O_{10})F_2$] and enstatite ($MgSiO_3$) by XRD study. This is furthermore confirmed from EDX pattern presented in Fig. 5. Spherical shaped crystallite particles (size ~ 100–500 nm) are predominated in NG-1 and NG-2 glass-ceramics and those possess density value ~2.59

and ~2.61 g cm^{-3}, respectively. As seen from Fig. 4c, the rock-like and plate-like crystallites are evenly distributed throughout the NG-3 glass-ceramic matrix to develop a compact microstructure. It can be seen that the rock-like particles mostly of nano size (~300–700 nm) are positioned (Fig. 4c) in fitted places between the plate shaped and card shaped crystallites of size range ~1–3 μm (Fig. 5a). Density of this glass-ceramic was estimated ~2.60 g cm^{-3}. The morphology of NG-4 glass-ceramic is very unique compare to other nanoparticle doped glass-ceramics. As is visual from Fig. 4d, various sized rock-like crystals are precipitated in the matrix and irregularly distributed to form a compact microstrutcure. Presence of hexagonal Au-nanoparticles in all over the place also increased the compactness and hence density (=~2.60 g cm^{-3}). It may be pointed out here that the density of silver and gold metals are 10.49 and 19.30 g cm^{-3} signifying that gold can fit itself in the ceramic domain with more mass in the same amount of volume rather than silver.[21,22] Hence, from the FESEM of NG-4 glass-ceramics, the crystallite size decreased, packing/compactness increased and density increased on small addition of Au- nanoparticles. Thus, *in situ* nanoparticle doped glass-ceramics (NG-1 & NG-2) possessed mostly spherical nanocrystallites whereas *ex situ* samples *i.e.* NG-3 and NG-4 contained rock shaped and plate shaped crystallites of micrometer range.[16,22]

3.4 Mechanical property of SiO_2–Al_2O_3–MgO–K_2O–B_2O_3–MgF_2 glass-ceramics

The mechanical property *i.e.* microhardness of four nano-particle doped SiO_2–Al_2O_3–MgO–K_2O–B_2O_3–MgF_2 glass-ceramics heat-treated at 950 °C have been evaluated by
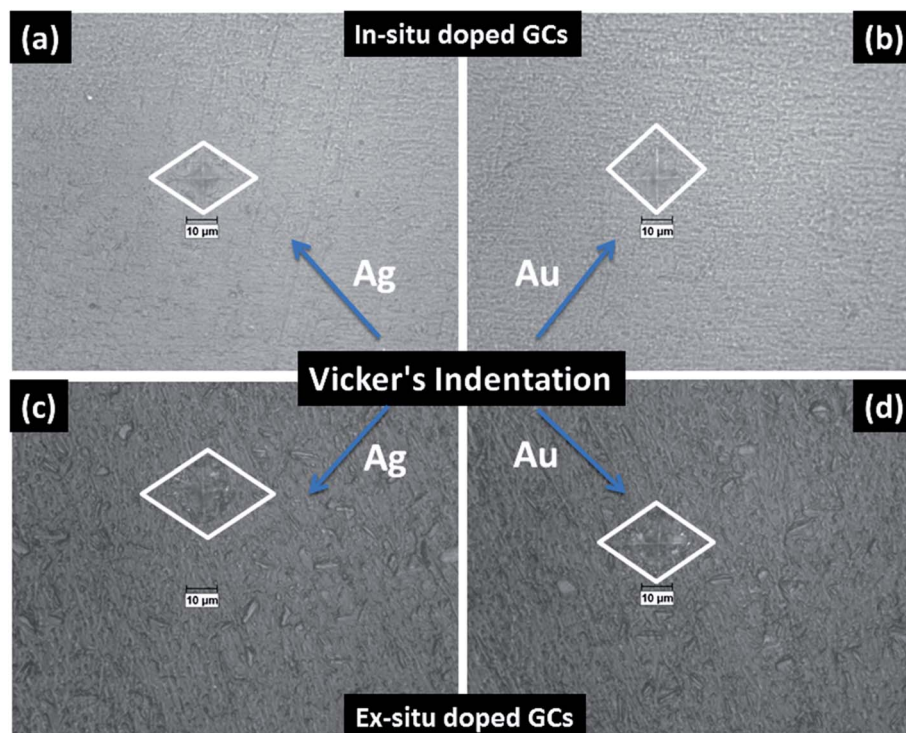
Fig. 6 Photomicrograph of Vickers indentation impression on SiO_2–Al_2O_3–MgO–K_2O–B_2O_3–MgF_2 glass-ceramics *i.e.* (a) NG-1, (b) NG-2, (c) NG-3 and (d) NG-4 heat-treated at 950 °C.

Vickers and Knoop indenters. Average of ten indentations was taken under indent load of 200 g each, using the average diagonal lengths of the hardness impressions. The images of the Vickers indentation impressions on glass-ceramics are depicted in Fig. 6. Over controlled heating at 950 °C, fluorophlogopite $[KMg_3(AlSi_3O_{10})F_2]$ crystals predominated in the ceramic matrix and for *ex situ* doped samples the crystallization is further supported. As depicted in Fig. 4a and b the spherical droplet-like nanocrystallites are precipitated predominantly in NG-1 and NG-2 glass-ceramics. The Vickers indentation impression on those two glass-ceramics is presented in Fig. 6a and b and microhardness value is estimated 4.48 ($\pm$0.13) and 4.61 ($\pm$0.14) GPa, respectively. In case of *ex situ* nanoparticle doped

samples, 1–3 μm sized plate shaped mica crystals predominated and thus, lower microhardness is obtained as 4.34 ($\pm$0.13) and 4.46 ($\pm$0.13) GPa for NG-3 and NG-4 glass-ceramics, respectively. The Vickers indentation impression on *ex situ* samples is presented in Fig. 6c and d. It is well established that the microhardness value of glass-ceramic directly depends on crystalline packing and corresponding microstructure developed after heat-treatment.[14,19] As already pointed out that the catalytic activity on crystallization was supported by Ag- and Au-nanoparticles because of close matching in lattice parameter, fine grained morphology is obtained in NG-3/NG-4 glass-ceramics. Lower microhradness of NG-3 & NG-4 glass-ceramics further ensured higher machinability (*m*) which was
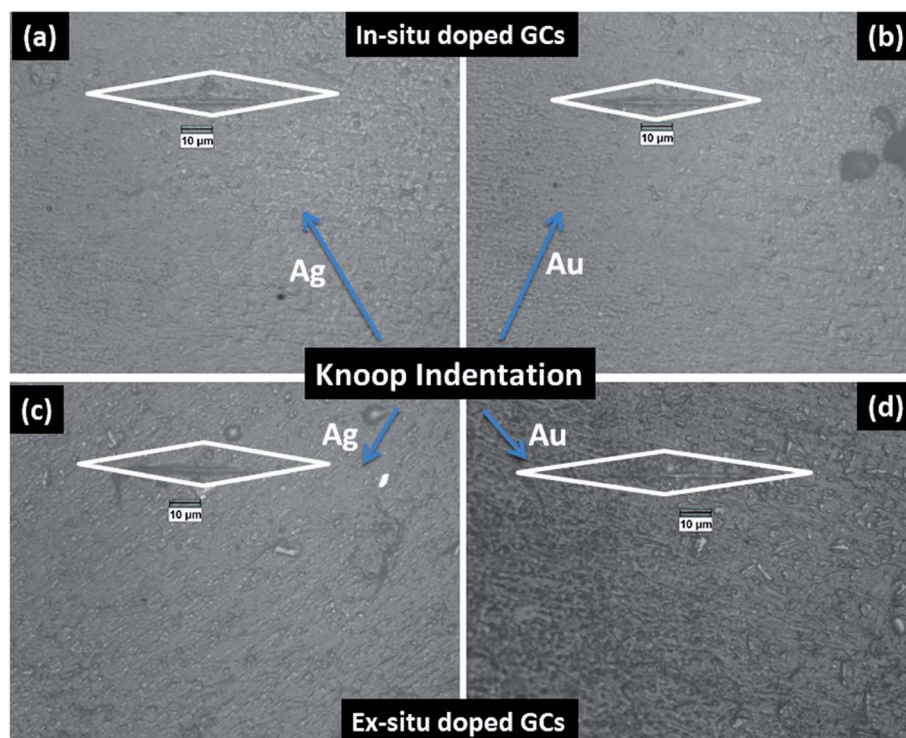
Fig. 7 Photomicrograph of Knoop indentation impression on $SiO_2–Al_2O_3–MgO–K_2O–B_2O_3–MgF_2$ glass-ceramics *i.e.* (a) NG-1, (b) NG-2, (c) NG-3 and (d) NG-4 heat-treated at 950 °C.

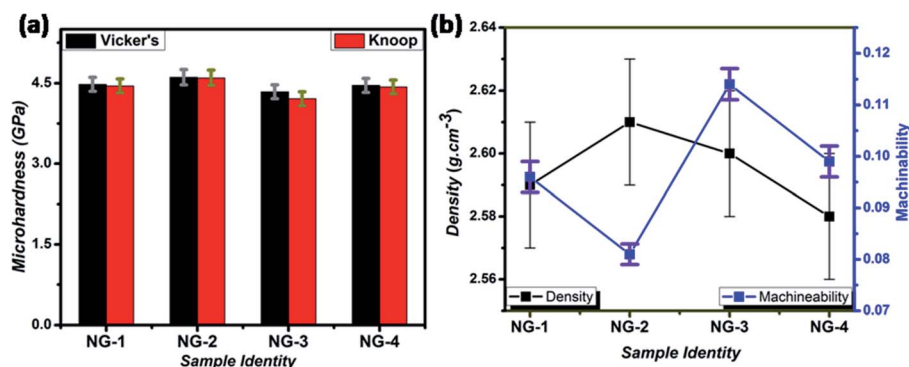**Fig. 8** Variation of Vickers & Knoop microhardness (a), and change of machinability & density (b) for different $SiO_2–Al_2O_3–MgO–K_2O–B_2O_3–MgF_2$ samples heat-treated at 950 °C.

determined using the eqn (1) *i.e.* $m = 0.643 − 0.122H$.[14] For NG-1 to NG-4 glass-ceramics, the machinability was estimated 0.096 (±0.003), 0.081 (±0.002), 0.113 (±0.003) and 0.099 (±0.003), respectively. Microhardness value estimated by Knoop indentation approach using same load for NG-1 to NG-4 glass-ceramics was 4.45 (±0.13), 4.60 (±0.14), 4.21 (±0.13) and 4.43 (±0.13) GPa, respectively. The Knoop indentation impression on NG-1 to NG-4 glass-ceramics is presented in Fig. 7a–d, respectively. Here it is seen that the microhardness value evaluated for each glass-ceramic using Vickers and Knoop method are close to each other (Fig. 8a). A correlation between machinability and density for glass-ceramics is projected in Fig. 8b. Except NG-2 system, the machinability directly corresponds to density. Hence in view of Fig. 8b it can be stated that easy machining is possible for *ex situ* Ag-nanoparticle doped $SiO_2–Al_2O_3–MgO–K_2O–B_2O_3–MgF_2$ glass-ceramics.

4. Conclusions

In this study, the comparative effects of *ex situ* and *in situ* generated silver and gold nanometals (0.2 wt% in excess) on crystallization behavior, thermal and mechanical properties of $SiO_2–MgO–Al_2O_3–B_2O_3–K_2O–MgF_2$ glass system have been investigated and the major findings are summarized below:

The effectiveness of silver (Ag) and gold (Au) nanoparticles on crystallization- and evolution of microstructure of heat-treated $SiO_2–MgO–Al_2O_3–B_2O_3–K_2O–MgF_2$ glass-ceramic and their mechanical properties is illustrated. Nanoparticles were doped *via* both *in situ* and *ex situ* mechanism and that was found to strongly affect the glass transition temperature (T_g) and crystallization temperature (T_c). *In situ* nanoparticle doped glasses with T_g value 622–630 °C showed similar density with *ex situ* doped glasses possessing T_g value 649–652 °C. Compare to *in situ* system, 90–110 °C increase in T_c was found for *ex situ* doped glasses (T_c = 870–875 °C).

Over controlled heat-treatment at 950 ± 10 °C, the glasses were converted into glass-ceramic (GC) with predominant crystalline phase (XRD) fluorophlogopite mica, [$KMg_3(AlSi_3O_{10})F_2$]. Along with the secondary phase enstatite ($MgSiO_3$), the presence of FCC Ag and Au particles were identified by XRD study.

Spherical crystallites of size ∼50–400 nm is observed through FE-SEM in *in situ* doped GCs. Whereas, *ex situ* Ag doped GC is composed of rock-like and plate-like crystallites mostly of size 1–3 μm ensured its superior machinability.

Vicker's and Knoop microhardness of *in situ* doped GCs were estimated within range of 4.45–4.61 GPa which reduced to 4.21–4.34 GPa in *ex situ* system. Machinability of GCs were found in the order, *ex situ* Ag > *ex situ* Au ∼ *in situ* Ag > *in situ* Au. Thus, the *ex situ* Ag/Au doped $SiO_2–MgO–Al_2O_3–B_2O_3–K_2O–MgF_2$ GC has potential for using as machinable glass-ceramic.

Conflicts of interest

There are no conflicts to declare.

References

1 G. H. Beall and L. L. Hench, in *Advances in Nucleation and Crystallization in Glasses*, ed. L. L. Hench and S. W. Freiman, Am. Ceram. Soc., Westerville, OH, 1971, pp. 251–261.

2 S. N. Hoda, Alkaline earth mica glass-ceramics, in *Nucleation Cryst. Glas.*, The American Ceramic Society, 1982, pp. 287–300.

3 Y. W. Park, J. W. Won and M. H. Yim, A study on the glass-ceramics of the fluorphlogopite system, *J. Korean Ceram. Soc.*, 1994, **31**(12), 1552–1560.

4 D. S. Baik, K. S. No, J. S. Chun and H. Y. Cho, Effect of the aspect ratio of mica crystals and crystallinity on the microhardness and machinability of mica glass-ceramics, *J. Mater. Process. Technol.*, 1997, **67**, 50–54, DOI: 10.1016/S0924-0136(96)02817-8.

5 J. Henry and R. G. Hill, Influence of alumina content on the nucleation crystallization and microstructure of barium fluorphlogopite glass-ceramics based on8SiO2·yAl2O3·4MgO·2MgF2·BaO: Part II - Microstructure, microhardness and machinability, *J. Mater. Sci.*, 2004, **39**, 2509–2515.

6 P. Alizadeh, B. EftekhariYekta and T. Javadi, Sintering behavior and mechanical properties of the mica-diopside machinable glass–ceramics, *J. Eur. Ceram. Soc.*, 2008, **28**, 1569–1573.

7 W. Höland and G. H. Beall, *Glass-Ceramic Technology*, John Wiley & Sons, New Jersey, 2nd edn, 2012, pp. 75–206, DOI: 10.1002/9781118265987.

8 M. Ghaffari, P. Alizadeh and M. R. Rahimipour, Sintering behavior and mechanical properties of mica-diopside glass–ceramic composites reinforced by nano and micro-sized zirconia particles, *J. Non-Cryst. Solids*, 2012, **358**(23), 3304–3311.

9 T. Behraznia, A. S. Alzahrani, M. Rashwan, A. J. Bushby and R. G. Hill, Machinability of fluormica glass-ceramics of high mica volume fraction, *J. Eur. Ceram. Soc.*, 2020, **40**(3), 887–892.

10 A. R. Molla and B. Basu, Microstructure, mechanical, and *in vitro* properties of mica glass-ceramics with varying fluorine content, *J. Mater. Sci.: Mater. Med.*, 2009, **20**, 869, DOI: 10.1007/s10856-008-3643-7.

11 H. Li, D. Q. You, C. R. Zhou and J. G. Ran, Study on machinable glass-ceramic containing fluorophlogopite for

dental CAD/CAM system, *J. Mater. Sci.: Mater. Med.*, 2006, 1133–1137, DOI: 10.1007/s10856-006-0540-9.

12 I. L. Denry and J. A. Holloway, Effect of heat pressing on the mechanical properties of a mica-based glass-ceramic, *J. Biomed. Mater. Res., Part B*, 2004, **70**, 37–42, DOI: 10.1002/jbm.b.30010.

13 S. Gali, K. Ravikumar, B. V. Murthy and B. Basu, Zirconia toughened mica glass ceramics for dental restorations, *Dent. Mater.*, 2018, **34**(3), e36–e45.

14 T. Behraznia, A. S. Alzahrani, R. Maher, A. J. Bushby and R. G. Hill, Machinability of fluormica glass-ceramics of high mica volume fraction, *J. Eur. Ceram. Soc.*, 2020, **40**(3), 887–892.

15 A. Mallik, P. K. Maiti, P. Kundu and A. Basumajumdar, Influence of B_2O_3 on Crystallization Behavior and Microstructure of Mica Glass-Ceramics in the System $BaO_4MgO \cdot Al_2O_3 \cdot 6SiO_2 \cdot 2MgF_2$, *J. Am. Ceram. Soc.*, 2012, **95**(11), 3505–3508.

16 M. Garai, T. S. R. C. Murthy and B. Karmakar, Microstructural characterization and wear properties of silver and gold nanoparticle doped K-Mg-Al-Si-OF glass-ceramics, *Ceram. Int.*, 2018, **44**, 22308–22317.

17 R. Casasola, J. M. Pérez and M. Romero, Crystal Growth of F-Phlogopite from Glasses of the SiO2–Al2O3–MgO–K2O–F System, *J. Am. Ceram. Soc.*, 2016, **99**(2), 484–491.

18 M. Garai, A. K. Maurya and S. Roy, Zn 2+-Controlled crystallization and microstructure in K-Li-Mg-B-Si-Al-F glass, *MRS Adv.*, 2018, **3**, 3525–3533.

19 K. Cheng, J. Wan and K. Liang, Enhanced Mechanical Properties of Oriented Mica Glass-ceramics, *Mater. Lett.*, 1999, **39**, 350–353.

20 M. Garai, N. Sasmal, A. R. Molla, S. P. Singh, A. Tarafder and B. Karmakar, Effects of nucleating agents on crystallization and microstructure of fluorophlogopite mica-containing glass-ceramics, *J. Mater. Sci.*, 2014, **49**, 1612–1623.

21 S. D. Stookey, Catalyzed crystallization of glass in theory and practice, *Ind. Eng. Chem.*, 1959, **51**, 805–808.

22 M. Garai, N. Sasmal, A. R. Molla, A. Tarafder and B. Karmakar, Effects of in situ generated coinage nanometals on crystallization and microstructure of fluorophlogopite mica containing glass-ceramics, *J. Mater. Sci. Technol.*, 2015, **31**, 110–115.

23 M. Garai and B. Karmakar, Rare earth ion controlled crystallization of mica glass-ceramics, *J. Alloys Compd.*, 2016, **678**, 360–369.

24 S. M. Salman, S. N. Salama and H. A. Abo-Mosallam, Contributions of CaO and SrO in crystallization and properties of some glasses based on stoichiometric tetra-silicic fluoromica, *Ceram. Int.*, 2017, **43**(12), 9424–9430.

25 R. W. Hopper, Stochastic Theory of Scattering from Idealized Spinodal Structures: II. Scattering in General and for the Basic Late Stage Model, *J. Non-Cryst. Solids*, 1985, **70**, 111–442.

26 B. Karmakar, T. Som, S. P. Singh and M. Nath, Nanometal-glass Hybrid Nanocomposites: Synthesis, Properties and Application, *Trans. Indian Ceram. Soc.*, 2010, **69**, 171–186.

27 K. Maeda and A. Yasumori, Effect of Molybdenum and Tungsten Oxides on Nucleation and Crystallization Behaviors of MgO–Al2O3–SiO2 Glasses, *J. Non-Cryst. Solids*, 2015, **427**, 152–159.